



TESTING RELATIVISTIC REFLECTION AND RESOLVING OUTFLOWS IN PG 1211+143 WITH *XMM-Newton* AND *NuSTAR*

A. P. LOBBAN¹, K. POUNDS¹, S. VAUGHAN¹, AND J. N. REEVES^{2,3}

¹ University of Leicester, Department of Physics and Astronomy, University Road, Leicester LE1 7RH, UK; al394@le.ac.uk

² Astrophysics Group, Keele University, Staffordshire, ST5 5BG, UK

³ Center for Space Science and Technology, 1000 Hilltop Circle, University of Maryland Baltimore County, Baltimore, MD 21250, USA

Received 2016 April 6; revised 2016 August 22; accepted 2016 September 5; published 2016 November 9

ABSTRACT

We analyze the broad-band X-ray spectrum (0.3–50 keV) of the luminous Seyfert 1/quasar PG 1211+143—the archetypal source for high-velocity X-ray outflows—using near-simultaneous *XMM-Newton* and *NuSTAR* observations. We compare pure relativistic reflection models with a model including the strong imprint of photoionized emission and absorption from a high-velocity wind, finding a spectral fit that extrapolates well over the higher photon energies covered by *NuSTAR*. Inclusion of the high signal-to-noise ratio *XMM-Newton* spectrum provides much tighter constraints on the model parameters, with a much harder photon index/lower reflection fraction compared to that from the *NuSTAR* data alone. We show that pure relativistic reflection models are not able to account for the spectral complexity of PG 1211+143 and that wind absorption models are strongly required to match the data in both the soft X-ray and Fe K spectral regions. In confirming the significance of previously reported ionized absorption features, the new analysis provides a further demonstration of the power of combining the high throughput and resolution of long-look *XMM-Newton* observations with the unprecedented spectral coverage of *NuSTAR*.

Key words: accretion, accretion disks – black hole physics – galaxies: active – galaxies: individual (PG 1211+143) – quasars: absorption lines

1. INTRODUCTION

The standard model of an active galactic nucleus (AGN) is driven by accretion onto a supermassive black hole (SMBH; $M_{\text{BH}} \sim 10^{6-9} M_{\odot}$). AGNs are powerful sources of X-rays which most likely originate close to the SMBH itself. The X-ray spectra of unobscured AGNs display an array of spectral features. In particular, they are often dominated by a hard power-law component, thought to be produced when ultraviolet photons, emitted from an optically thick, geometrically thin accretion disc (Shakura & Sunyaev 1973), are inverse-Compton scattered by a “corona” of hot electrons (Haardt & Maraschi 1993). Additional spectral features typically include a soft excess < 2 keV (Scott et al. 2012), a “Compton reflection” component > 10 keV (Nandra & Pounds 1994) and emission lines, the strongest of which is often Fe K α fluorescence at ~ 6.4 keV (George & Fabian 1991).

Through systematic spectral studies with *ASCA*, *XMM-Newton*, *Chandra* and *Suzaku*, a significant fraction of AGNs are now routinely observed to also exhibit strong signatures of ionized absorption in their X-ray spectra, with at least half of all AGNs hosting photoionized “warm” absorbers (e.g., Reynolds & Fabian 1995; Blustin et al. 2005). These absorbers produce numerous narrow and blueshifted absorption features (e.g., Kaspi et al. 2002; Crenshaw et al. 2003; McKernan et al. 2007), implying material outflowing at a velocity from several hundred to several thousand km s^{-1} .

Through the study of blueshifted absorption lines of K-shell Fe, observations of higher-luminosity AGNs have also revealed the presence of much more highly ionized absorbers originating in high-velocity disc winds ($v_{\text{out}} \sim 0.1c$; e.g., PG 1211+143; Pounds et al. 2003, PDS 456; Reeves et al. 2003). Subsequent studies of archival *XMM-Newton* and *Suzaku* data have shown that similar high-velocity, highly-ionized outflows may be relatively common in nearby, luminous AGNs (e.g., Tombesi

et al. 2010, 2011; Gofford et al. 2013). In general, the derived outflow rates are comparable to the AGN accretion rate (up to several solar masses per year) and carry kinetic power on the order of a few percent of the bolometric luminosity. Such high-velocity outflows are believed to play a key role in linking growth of the SMBH and the host galaxy (King 2003, 2010) and offer an appealing explanation for the observed M – σ relation for galaxies (Ferrarese & Merritt 2000; Gebhardt 2000).

The archetypal high-velocity-outflow source is PG 1211+143, a luminous narrow-line Seyfert galaxy/quasar at a redshift of $z = 0.0809$ (Marziani et al. 1996), which is both optically bright with a strong “big blue bump” and X-ray bright with a typical X-ray luminosity of $\sim 10^{44}$ erg s^{-1} . The source is well-known for its spectral complexity and, through an *XMM-Newton* observation in 2001, provided the first detection of a sub-relativistic outflow ($v_{\text{out}} \sim 0.14c$) in a non-broad absorption line AGN (Pounds et al. 2003; Pounds & Page 2006).

Subsequent *XMM-Newton* observations of PG 1211+143 were combined to model the photoionized absorption and emission spectra, quantifying the mass flux and energetics of the outflow and confirming the potential importance for galaxy feedback (Pounds & Reeves 2007, 2009; Pounds 2014). An extended *XMM-Newton* observation in 2014 has since shown the highly-ionized wind to have several outflow components, with primary velocities of $v_{\text{out}} \sim 0.066c$ and $\sim 0.129c$ (Pounds et al. 2016a).

Surprisingly, the analysis of a 2014 *NuSTAR* observation of PG 1211+143 (Zoghbi et al. 2015) found no evidence for the high-velocity outflow, leading to the suggestion that it may be a variable, transient feature—a result which would have important implications for the prevalence of high-velocity outflows in high-luminosity AGNs and their wider significance for feedback. Here, we report on a combined analysis of the

same *NuSTAR* data with the contemporaneous extended ~ 630 ks *XMM-Newton* observation obtained in 2014.

2. OBSERVATIONS AND DATA REDUCTION

PG 1211+143 was observed by *NuSTAR* (Harrison et al. 2013) four times in 2014: February 18 (ID: 60001100002), April 8 (60001100004), April 9 (60001100005) and July 7 (60001100007; hereafter *Nu7*), with exposure times of 111, 48, 64 and 74 ks, respectively. We used the NUPIPELINE and NUPRODUCTS scripts, as part of HEASOFT v6.17,⁴ to extract spectral products using the latest calibration database (version 20151008). We extracted spectral products from circular source regions with radii of 52 arcsec while background products were extracted from two same-sized circular regions separate from the source and away from the edges of the CCD. We analyzed spectra from both of *NuSTAR*'s Focal Plane Modules (FPMA and FPMB) using XSPEC v12.9.0 (Arnaud 1996). We find that the *NuSTAR* spectra become heavily background-dominated at >30 keV, resulting in the high-energy data becoming very noisy. As such, we binned each individual spectrum in terms of signal-to-noise ratio (S/N), ensuring that each spectral bin is detected at the $\geq 3\sigma$ level, which also allows us to use χ^2 minimization. We analyzed all FPMA and FPMB spectra simultaneously, allowing for a floating cross-normalization parameter. Typically, the cross-calibration normalization of the FPMB relative to the FPMA is 1.01 ± 0.03 , consistent with the cross-calibration results presented in Madsen et al. (2015). The FPMA+FPMB background-subtracted 3–50 keV count rates of the four *NuSTAR* observations are ~ 0.14 , ~ 0.19 , ~ 0.21 and ~ 0.14 ct s^{-1} , respectively. This corresponds to respective 3–50 keV observed fluxes of ~ 6.4 , ~ 8.4 , ~ 9.2 and $\sim 6.6 \times 10^{-12}$ $\text{erg cm}^{-2} \text{s}^{-1}$.

PG 1211+143 was also observed with *XMM-Newton* (Jansen et al. 2001) on seven occasions in 2014 from June 2 to July 7, with a total exposure of ~ 630 ks. The details of the observations and their subsequent data reduction are described in Lobban et al. (2016). We note that the *XMM-Newton* spectra are binned up such that there are >100 ct bin^{-1} . Here, we primarily focus on the fourth *NuSTAR* observation (referred to as *Nu7*), as this overlapped with the *XMM-Newton* campaign and was directly simultaneous with the final *XMM-Newton* observation (rev2670). The four separate *NuSTAR* lightcurves are shown in Zoghbi et al. (2015). The upper panel of Figure 1 shows the *Nu7* lightcurve,⁵ while the lower panel shows the rev2670 *XMM-Newton* European Photon Imaging Camera (EPIC)-pn lightcurve in the 3–10 keV energy band, demonstrating how the hard X-ray variability matches up. However, given the lack of significant within-observation spectral variability at high energies, we proceed to analyze the time-averaged spectra.

3. SPECTRAL ANALYSIS

In Pounds et al. (2016a, 2016b), we reported the analysis of an extended *XMM-Newton* observation of PG 1211+143, modeling both hard (2–10 keV) spectra from the EPIC-pn camera (Strüder et al. 2001) and higher-resolution soft (<2

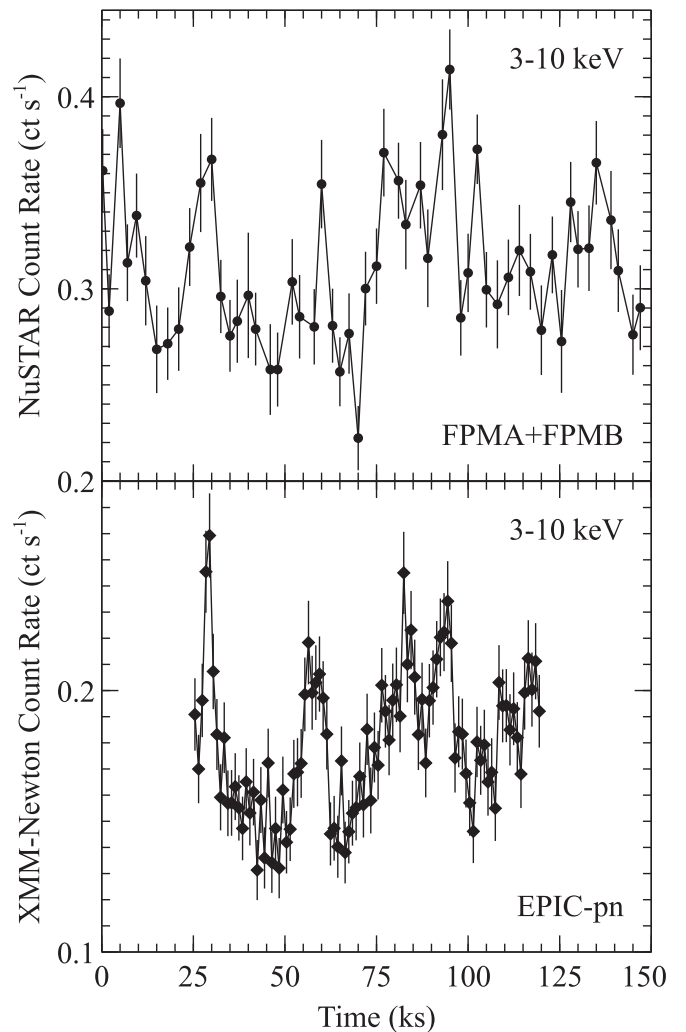


Figure 1. Upper panel: the *Nu7* FPMA+FPMB *NuSTAR* lightcurve from 3–10 keV in 2 ks bins. The plotted count rate has been corrected using the NULCCORR task. Lower panel: the simultaneous rev2670 *XMM-Newton* EPIC-pn lightcurve from 3 to 10 keV in 1 ks bins.

keV) spectra from the Reflection Grating Spectrometer (RGS; den Herder et al. 2001) with XSTAR (Kallman et al. 1996). We generated a set of self-consistent custom-built XSTAR grids with the correct ionizing continuum for PG 1211+143, based on a spectral energy distribution model described in Lobban et al. (2016). The grids were based on the abundances of Grevesse & Sauval (1998). We identified several components of ionized outflowing material, both confirming the presence of the high-velocity, sub-relativistic component ($\sim 0.14c$) first detected in Pounds et al. (2003) and detecting additional lower-velocity components. The continuum was modeled by a hard power law ($\Gamma \sim 1.7$ – 1.8) with a blackbody component and softer “unabsorbed” power law ($\Gamma \sim 3$) dominating <1 keV. The softer power-law component is largely responsible for the long-term spectral variability observed on timescales of \sim days (see Lobban et al. 2016). We return to this model in Section 3.3.

Through the acquisition of contemporaneous *NuSTAR* observations, Zoghbi et al. (2015) independently modeled the hard 3–50 keV spectrum of PG 1211+143. They combined the data from both the FPMA and FPMB from all four observations in 2014. Their best-fitting model comprised a

⁴ <https://heasarc.gsfc.nasa.gov/lheasoft/>

⁵ Note that the *NuSTAR* count rate has been adjusted via various corrections as part of the NULCCORR task. These include corrections for the “live time,” point-spread function, vignetting, etc.

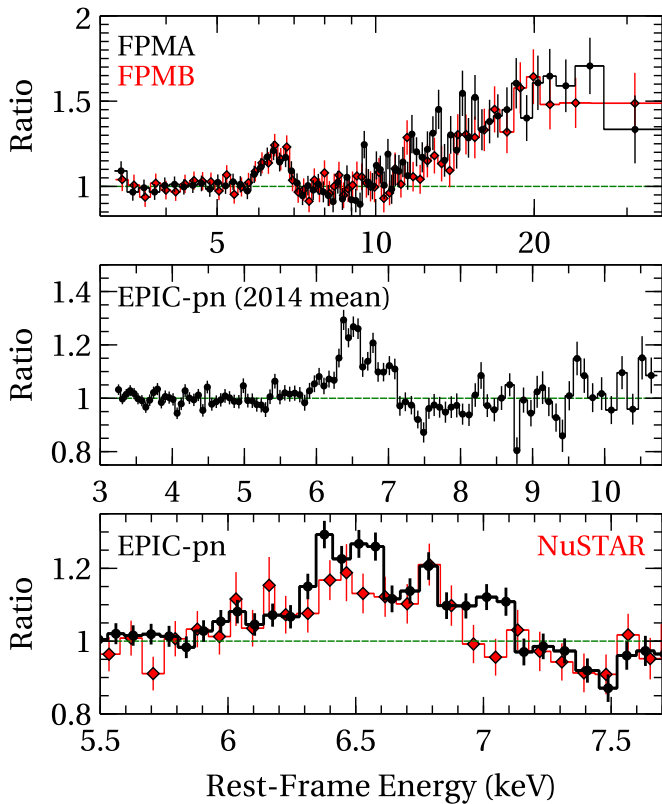


Figure 2. The residuals of the co-added *NuSTAR* (upper panel) and *XMM-Newton* EPIC-pn (middle panel) spectra as a ratio to an absorbed power law fitted from 3–5 + 7.5–10 keV. The lower panel shows a zoom-in of the Fe K region in both the EPIC-pn (black) and combined *NuSTAR* (red) spectra.

single, steep power law ($\Gamma = 2.5 \pm 0.2$) plus strong emission from relativistic reflection, which accounts for the component of Fe K emission at ~ 6 –7 keV and an excess of hard emission > 10 keV, modeled using RELXILL⁶ (Dauser et al. 2013). The reflection emission is strong, with $R = 2.5$ –4.5,⁷ but the Fe abundance is sub-solar ($A_{\text{Fe}} = 0.7 \pm 0.1$) to compensate for the weak Fe K line (relative to the reflection continuum). And, highly relevant to our current study, they found no requirement for any signatures of high-velocity absorption. In Figure 2, we show the *NuSTAR* and *XMM-Newton* EPIC-pn residuals to a simple power-law fit. The middle/lower panels highlight the structure in the Fe K band in the EPIC-pn spectrum, which spectral modeling finds to be consistent with contributions from narrow near-neutral Fe K α , Fe XXV $1s$ – $2p$ resonance and Fe XXVI Ly α emission lines at 6.4, 6.7 and 6.97 keV, respectively. Additionally, absorption structure is visible at ~ 7.5 keV. In contrast, the *NuSTAR* spectra do not resolve this contribution from narrower absorption/emission lines, with a smoother profile being observed. This may be due to the difference in resolution between *XMM-Newton* and *NuSTAR* at Fe K, although the apparent lack of Fe XXVI emission at ~ 6.97 keV in the *NuSTAR* spectra may also arise from the

⁶ <http://www.sternwarte.uni-erlangen.de/~dauser/research/relxill/>

⁷ The reflection fraction, R , is typically thought of as a proxy for the strength of the reflection component, where a value $R = 1$ corresponds to “standard” reflection from a semi-infinite disc covering 2π sr, assuming a static corona.

effects of variability, given that the co-added *NuSTAR* observations span a time period of approximately five months.

All our subsequent fits include a Galactic column of $N_{\text{H}}^{\text{Gal}} = 3.06 \times 10^{20} \text{ cm}^{-2}$ (Willingale & Starling 2013), modeled with the TBABS code within XSPEC, using the abundances of Wilms et al. (2000) and the absorption cross-sections of Verner et al. (1996). In our broad-band EPIC-pn fits we ignore the 1.7–2.35 keV band (observed frame; rest-frame ~ 1.8 –2.5 keV) due to calibration uncertainties around the Si and Au detector edges at ~ 1.8 and ~ 2.2 keV, respectively. All errors are quoted at the 90% level for one parameter of interest (i.e., $\Delta\chi^2 = 2.71$), unless stated otherwise.

3.1. Fitting the Hard X-Ray Spectrum with a Relativistic Reflection Model

In this section, we detail the results of fitting the hard X-ray spectrum with RELXILL, a relativistic reflection model. We use an up-to-date version of RELXILL, namely v0.4a (dated 2016 January 18), with the newly implemented reflection fraction parameter, R . Previous versions of RELXILL used an alternative definition of R , as discussed in Dauser et al. (2016). The interesting parameters in the RELXILL model are the photon index, Γ , reflection scaling fraction, R (defined above), abundance of Fe relative to solar values, A_{Fe} (assuming the abundances of Grevesse & Sauval 1998), emissivity index, q , dimensionless black hole spin, a^* , inclination angle of the inner disc, θ , inner and outer radii of emission, r_{in} and r_{out} , respectively, ionization parameter⁸, ξ , and high-energy cutoff, E_{cut} , in units of keV. Note that r_{in} and r_{out} can be computed in units of r_g (where $r_g = GM/c^2$) or in units of the innermost stable circular orbit (ISCO; which is dependent on a^*). In all fits, we fixed r_{out} at the default value $400 r_g$, as the fits are insensitive to the parameter and, as per Zoghbi et al. (2015), we assume that q takes the form of a single power law.

We first fitted the co-added⁹ FPMA and FPMB *NuSTAR* spectra with RELXILL (where RELXILL models both an absorbed power law and the relativistic reflection component), and obtained parameters consistent with those of Zoghbi et al. (2015) and a fit statistic of $\chi^2_{\text{dof}} = 563/520$ (dof = degrees of freedom). We also found consistent results by fitting all four *NuSTAR* spectra simultaneously, allowing for a floating cross-normalization parameter to account for flux variability between observations ($\chi^2_{\text{dof}} = 2089/2162$). As per Zoghbi et al. (2015), we find that q is degenerate with r_{in} . Additionally, we find no significant change in the fit between fixing a^* at 0 (stationary) or 0.998 (maximal spin). The *NuSTAR* spectra begin to become background-dominated > 30 keV and the spectrum becomes very noisy—however, we fit up to 50 keV here for comparison with Zoghbi et al. (2015).

We investigated the co-dependence of the parameters in this reflection model using a Markov Chain Monte Carlo (MCMC) method to explore the multi-dimensional parameter space. Specifically, we used the CHAIN command within XSPEC, using the Goodman–Weare algorithm and 200 walkers, where each chain contains a total of 10^6 samples. The output allowed us to

⁸ The ionization parameter is defined as $\xi = L_{\text{ion}}/nr^2$, where L_{ion} is the ionizing luminosity from 1 to 1000 Rydberg, n is the gas density in units of cm^{-3} and r is the distance in units of cm. The parameter has units of erg cm s^{-1} .

⁹ The co-added spectra were created with the ADDSPEC code, as part of the HEASOFT suite, and were grouped in terms of S/N, such that each bin is detected at the $\geq 5\sigma$ level.

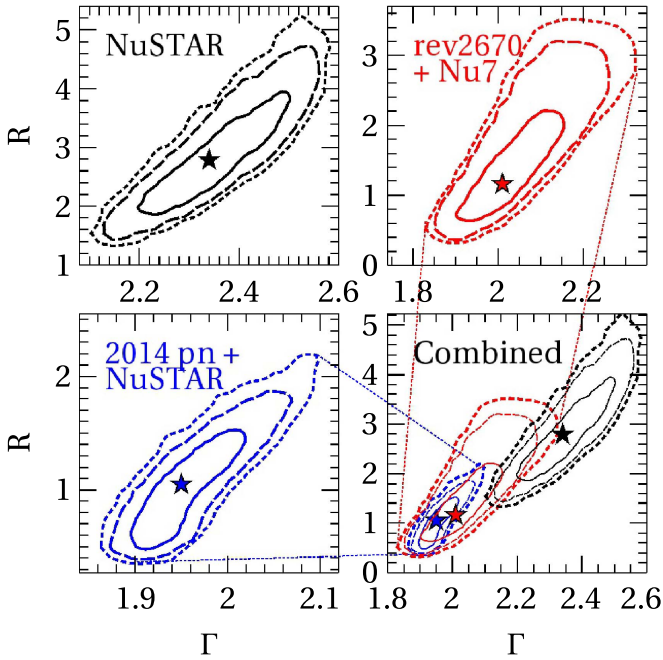


Figure 3. 2D density plots comparing Γ and R for the co-added *NuSTAR* spectrum (upper-left; black), the rev2670 EPIC-pn + *Nu7* spectrum (upper-right; red) and the mean 2014 EPIC-pn + co-added *NuSTAR* spectrum (lower-left; blue) from a fit with RELXILL in the 3–50 keV energy band. The bottom-right panel shows the three contour plots superimposed on one another. The projections were computed from a 10^6 -length MCMC run. The inner to outer shaded contours contain 68.3%, 95.5% and 99.7% of the total sample mass, respectively, and the stars represent the best-fitting values from the spectral fits.

plot the regions of high likelihood for each parameter.¹⁰ Specifically, we used the CORNER¹¹ routine within the PYTHON¹² programming language to create 1D histograms and 2D density plots, comparing all free parameters, and ensuring that our fits were not stuck in any local minima.

In Figure 3, we show a 2D density plot comparing Γ and R for the co-added *NuSTAR* spectrum (upper-left panel; black). The three contour levels, from inner to outer, contain 68.3% (solid line), 95.5% (dashed line) and 99.7% (dotted line) of the total mass (i.e., the 1σ , 2σ and 3σ levels for a Gaussian distribution). A steep Γ /high R solution is preferred: $\Gamma = 2.35_{-0.15}^{+0.16}$; $R = 2.79_{-0.91}^{+1.37}$, where the MCMC output is used to estimate the 90% uncertainties on our fit parameters. Meanwhile, the fit prefers a sub-solar Fe abundance: $A_{\text{Fe}} = 0.86_{-0.24}^{+0.83}$. The best-fitting values are summarized in Table 1.

The upper-right and lower-left panels of Figure 3 (red, blue) show the MCMC output when RELXILL is applied to: (i) the simultaneous rev2670 *XMM-Newton* EPIC-pn + *Nu7* *NuSTAR* spectrum, and (ii) the total co-added 2014 EPIC-pn + *NuSTAR* spectrum from 3 to 50 keV. The advantage of this approach is that the high resolution/throughput afforded by the EPIC-pn <10 keV allows for better constraints on the continuum and Fe K emission complex. While case (i) provides us with a spectrum totally free from the uncertainties arising from long-term spectral variability, case (ii) affords us the highest S/N in a PG 1211+143 spectrum to date, with a combined ~ 930 ks of

contemporaneous data. Fitting the co-added spectrum is justified on the basis of the long-term X-ray variability being relatively weak >3 keV (see Zoghbi et al. 2015; Lobban et al. 2016). All parameters were tied together between spectra except for the relative normalizations. In the simultaneous fit [i.e., case (i)], the *XMM-Newton* and *NuSTAR* normalizations were found to be within $\pm 2\%$ of each other.

The inclusion of the EPIC-pn data places much tighter constraints on Γ and R , with a harder- Γ /lower- R solution now preferred. If we fix the photon index at $\Gamma = 2.51$, as per the value reported by Zoghbi et al. (2015) from a fit to the *NuSTAR* data alone, we find that this is now rejected ($\Delta\chi^2 = 35$), despite R increasing to ~ 5 and A_{Fe} dropping to ~ 0.4 to compensate for the photon index being forced to a steeper value. These tighter constraints help to demonstrate the power of combining the high throughput of the EPIC-pn camera with the broad-band coverage and unprecedented sensitivity >10 keV of *NuSTAR*.

Finally, untying Γ between data sets improves the fit in case (ii) ($\Delta\chi^2 \sim 60$ with the value steepening in the *NuSTAR* spectrum by $\Delta\Gamma = 0.1$), most likely due to between-observation spectral variability, but not in case (i), with $\Gamma = 2.00 \pm 0.07$ for the *XMM-Newton* EPIC-pn and $\Gamma = 2.02 \pm 0.11$ for the simultaneous *NuSTAR* spectrum. This difference of $\Delta\Gamma = 0.02$ lies within the cross-calibration uncertainties presented in Madsen et al. (2015). Allowing Γ to vary between data sets does not have any significant impact on R in case (i). In case (ii), R is found to increase slightly ($\Delta R = 0.07$, with A_{Fe} dropping to ~ 1 so as not to over-predict the Fe line), although this is still within the statistical uncertainties of the parameter and does not alter our conclusions. None of the other parameters is significantly affected. All free parameters and fit statistics are summarized in Table 1.

3.2. Fitting the Broad-band Spectrum with Relativistic Reflection

While a relativistic reflection model provides a reasonable fit to the 3–50 keV X-ray spectrum, in Figure 4 we show the effect of extrapolating this model down to 0.3 keV (panel (a)). It is clear that the fit to the hard X-ray spectrum dramatically under-predicts the flux at low energies. Here, we initially focus on the simultaneous rev2670 EPIC-pn + *Nu7* spectrum. Re-fitting the reflection model to the 0.3–50 keV spectrum, the high-S/N soft X-ray spectral region drives the fit, returning Γ and R to higher values of ~ 2.4 and ~ 5 , respectively, and pushing the emissivity up to $q \sim 5$ and a^* to maximal spin with most of the emission arising from the ISCO. This produces a strong, relatively smooth soft excess <2 keV, but such strong relativistic blurring blends the Fe K emission complex into the continuum. This leaves significant residuals and results in a relatively poor fit: $\chi^2_{\text{dof}} = 1174/1003$ (panel (b)) and $\chi^2_{\text{dof}} = 239/127$ in the Fe K band (5.5–7.5 keV).

Panel (c) of Figure 4 shows the σ -residuals of a dual-reflector fit, incorporating additional emission from a non-relativistic distant reflector using the XILLVER model of García et al. (2014), tying Γ , A_{Fe} , θ and E_{cut} to the corresponding RELXILL parameters. The ionization parameter of the XILLVER component is consistent with zero as it matches fluorescent emission from Fe K α while modeling additional Compton reflection from optically-thick material. The addition of this component improves the fit by $\Delta\chi^2 = 55$, although the fit in the soft band

¹⁰ If interpreted in Bayesian terms, we map the posterior density, implicitly assuming uniform priors on each fitted parameter.

¹¹ <https://zenodo.org/record/11020#.Vs75hYyLR0t>

¹² <https://www.python.org/>

Table 1
The Best-fitting Values from Our 3–50 keV Fits with RELXILL

Dataset (3–50 keV)	Γ	R	A_{Fe}	q	θ ($^{\circ}$)	$\log \xi$	r_{in} (r_g)	a^*	E_{cut} (keV)	χ^2_{dof}
Co-added <i>NuSTAR</i>	$2.35^{+0.16}_{-0.15}$	$2.79^{+1.37}_{-0.91}$	$0.86^{+0.83}_{-0.24}$	$2.1^{+4.8}_{-1.3}$	36^{+13}_{-6}	$1.12^{+0.38}_{-0.98}$	<20	...	130^{+130}_{-36}	563/520
rev2670+ <i>Nu7</i>	$2.01^{+0.18}_{-0.08}$	$1.16^{+1.11}_{-0.40}$	$2.04^{+1.98}_{-1.05}$	$1.9^{+6.1}_{-1.1}$	36^{+12}_{-6}	$1.95^{+0.31}_{-1.85}$	<90	...	>110	673/662
2014-mean-pn + <i>NuSTAR</i>	$1.95^{+0.07}_{-0.05}$	$1.05^{+0.47}_{-0.49}$	$1.70^{+0.77}_{-0.77}$	$1.6^{+0.4}_{-0.7}$	40^{+7}_{-7}	$1.10^{+1.39}_{-0.76}$	<29	...	75^{+45}_{-24}	1 510/1 237

Note. A dash (“–”) means that we are unable to obtain useful constraints on that parameter. The 90% uncertainties on the parameters are estimated from our MCMC output.

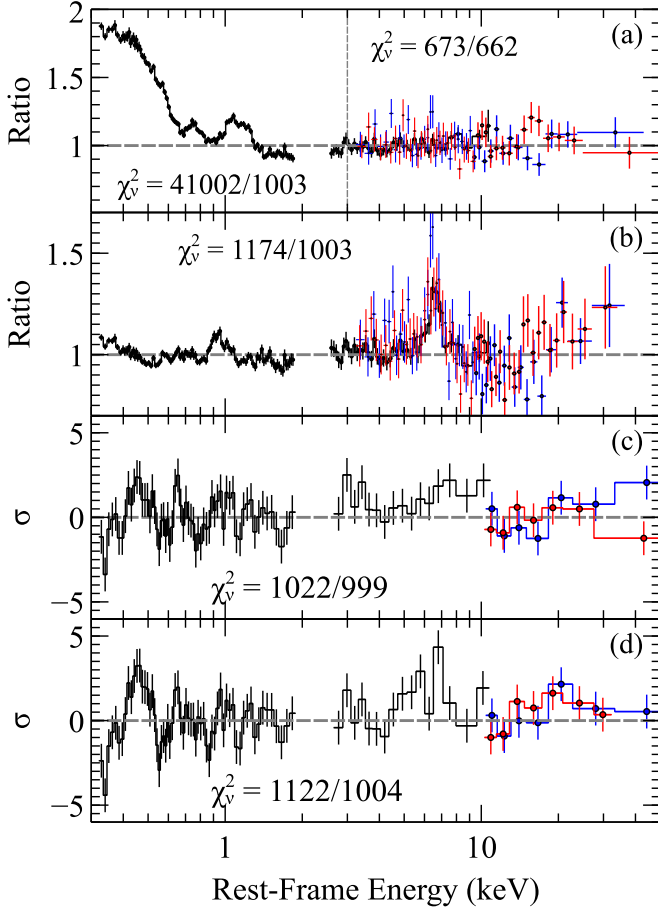


Figure 4. Panel (a): an extrapolation of the RELXILL fit to low energies (rev2670 EPIC-pn = black; *Nu7* FPMA = red; *Nu7* FPMB = blue). Panel (b): fitting the broad-band spectrum with RELXILL. Panels (c) and (d) show the RELXILL + XILLVER + PL_{soft} vs. PL_{hard} + XILLVER + PL_{soft} residuals, respectively. The *NuSTAR* data are only plotted >10 keV in the lower panels. This is for clarity as it allows the residuals of the two models to be better visually compared from 3 to 10 keV where the FPMA and FPMB overlap with the EPIC-pn.

is still poor. As such, we also include an additional steep power-law component ($\Delta\chi^2 = 97$), accounting for a component of soft excess, as was required by the RGS analysis of Pounds et al. (2016b). The steep component is the dominant source of long-term spectral variability (e.g., see the difference spectrum in Lobban et al. 2016).

Meanwhile, panel (d) of Figure 4 shows the σ -residuals to a broad-band fit with no relativistic reflection (i.e., with the hard and soft power laws plus the distant, near-neutral reflector). This helps to visualize which spectral components the relativistic reflector is modeling. It appears that the residuals

are very similar in the two cases, with an exception at the Fe K complex, where RELXILL models some excess emission from ~ 5.5 to 7 keV. Some of this excess emission may arise from a broadened component of emission, although some of the residuals, particularly in the EPIC-pn spectrum, may be accounted for with additional narrow emission lines (i.e., see Pounds et al. 2016a where the stacked EPIC-pn spectrum resolves the Fe K emission complex consisting of Fe K α fluorescence plus resonance lines from He-like (~ 6.7 keV) and H-like (~ 6.97 keV) Fe (see Figure 2; lower panel), which are well modeled with photoionized absorption and may represent scattering of the wind). Overall, the dual-reflector model gives an acceptable fit to the simultaneous broad-band spectrum: $\chi^2_{\text{dof}} = 1 022/999$. The best-fitting parameters are detailed in Table 2.

We also apply the same model to the mean EPIC-pn + *NuSTAR* spectrum, including all four *NuSTAR* observations separately, accounting for changes in flux over time with a floating cross-normalization parameter. The final fit statistic is $\chi^2_{\text{dof}} = 3573/3302$, where we have also allowed Γ to vary between *NuSTAR* observations. The best-fitting parameters are detailed in Table 2. Figure 5 shows the effect of fitting the dual-reflector model to the mean EPIC-pn spectrum. With the increased S/N afforded by ~ 630 ks of data, strong residuals are now apparent in the spectrum ($\chi^2_{\text{dof}} = 1454/1120$). In particular, there is clear evidence of ionized absorption from ~ 0.5 to 0.9 keV plus an excess of positive residuals just blueward of the peak of the Fe K emission complex (i.e., >6.4 keV). This is most likely the signature of the narrow He-like/H-like resonance lines from Fe reported in Pounds et al. (2016a). Additionally, there are significant negative residuals at ~ 7.5 keV, which is a signature of the highest-velocity component of the fast outflow ($v \sim 0.13c$; see Pounds et al. 2016a). Indeed, the fit is very poor in these bands: 0.5–0.9 keV: $\chi^2_{\text{dof}} = 181/68$; 5.5–7.5 keV: $\chi^2_{\text{dof}} = 233/165$. In summary of this section, we find that combining *XMM-Newton* and *NuSTAR* spectra shows that a model based on reflection alone cannot reproduce all of the observed spectral features without including the now well-established ionized emission and absorption in both the Fe K and soft X-ray bands.

3.3. An Alternative Fit to the Broad-band Spectrum with an Ionized Absorption Model

In this section, we demonstrate an alternative approach with a model incorporating the ionized wind parameters from Pounds et al. (2016a, 2016b) to form a broad-band model which we now fit to the combined *XMM-Newton*+*NuSTAR* spectrum. As noted above, those two papers report on analyses of the EPIC-pn hard X-ray band and the soft RGS band, respectively. In the former case, the 2–10 keV baseline X-ray

Table 2

The Best-fitting Values from Our Broad-band 0.3–50 keV Fits with the Dual-reflector Model Described in Section 3.2

Model (Statistic)	Component	rev2670 + <i>Nu7</i>	2014-mean-pn + <i>NuSTAR</i>
RELXILL	Γ	$2.21^{+0.05}_{-0.06}$	$2.20^{+0.02}_{-0.02}$
	R	$4.48^{+0.54}_{-1.88}$	$4.33^{+0.55}_{-0.40}$
	A_{Fe}	$2.11^{+0.38}_{-0.42}$	$1.35^{+0.22}_{-0.24}$
	q	$3.6^{+0.5}_{-0.7}$	$4.0^{+0.5}_{-0.3}$
	θ ($^\circ$)	44^{+4}_{-6}	44^{+2}_{-2}
	$\log \xi$	$1.00^{+0.07}_{-0.13}$	$1.17^{+0.08}_{-0.06}$
	r_{in} (r_g)	<3.3	<2.0
	a^*	>0.69	>0.97
	E_{cut} (keV)	130^{+80}_{-60}	>150
	$\log(N)$	$-4.81^{+0.04}_{-0.05}$	$-4.73^{+0.03}_{-0.02}$
XILLVER	Γ	2.21^\dagger	2.26^\dagger
	A_{Fe}	2.11^\dagger	1.35^\dagger
	θ ($^\circ$)	44^\dagger	44^\dagger
	$\log \xi$	<0.13	<0.03
	E_{cut} (keV)	130^\dagger	$>150^\dagger$
	$\log(N)$	$-5.42^{+0.15}_{-0.26}$	$-5.36^{+0.14}_{-0.11}$
	$\Delta\chi^2$	55	99
	$\Delta\chi^2$		
PL _{soft}	Γ	$3.56^{+0.24}_{-0.08}$	$3.66^{+0.12}_{-0.11}$
	$\log(N)$	$-3.41^{+0.10}_{-0.11}$	$-3.59^{+0.11}_{-0.05}$
	$\Delta\chi^2$	97	413
Fit statistic	χ^2_{dof}	1022/999	3573/3302

Note. Note that Γ , A_{Fe} , θ and E_{cut} are tied between the RELXILL and XILLVER models (denoted by †), while “ $\log(N)$ ” refers to the normalization of the model component, where the normalization is in units of $\text{photon cm}^{-2} \text{s}^{-1}$. The quoted value of Γ in the right-hand column was obtained from the EPIC-pn spectrum; the *NuSTAR* Values are typically around $\Gamma \sim 2.3$. The $\Delta\chi^2$ values refer to the improvement in the fit statistic upon sequentially adding the model components (i.e., RELXILL vs. RELXILL + XILLVER and RELXILL + XILLVER vs. RELXILL + XILLVER + PL_{soft}, respectively).

continuum is dominated by a hard power law ($\Gamma \sim 1.7$) with multiple blueshifted absorption lines corresponding to two ionized outflow components, with parameters of $\log \xi = 4.0$ and 3.4 , $N_{\text{H}} = 3.7$ and $2.0 \times 10^{23} \text{ cm}^{-2}$ and $v_{\text{out}} = 0.129$ and $0.066c$, respectively, when modeled with XSTAR (Kallman et al. 1996). The near-neutral Fe $K\alpha$ fluorescence line at 6.4 keV is modeled together with a modest reflection continuum using a distant reflector (XILLVER), whose photon index is tied to that of the hard power law. Additional XSTAR emission grids model ionized emission lines at ~ 6.7 and ~ 6.97 keV, identified with He-like and H-like Fe $1s-2p$ resonance transitions.

The baseline continuum for the RGS analysis (0.3–2 keV) is dominated by the well-known “soft excess,” with both ionized emission and absorption features being imprinted on a blackbody component ($kT \sim 0.1$ keV). An additional soft power law ($\Gamma \sim 2.9$), found in inter-orbit difference spectra (Lobban et al. 2016), matches the variable component of the soft excess and is included in the model. The analysis by Pounds et al. (2016b) finds evidence for several outflow components, ranging in $\log \xi$ from 1.5–3.2 and N_{H} from 1.5 to $28 \times 10^{20} \text{ cm}^{-2}$, with lower-ionization/lower-column-density counterparts apparently co-moving with the dual-velocity outflow components detected in the hard X-ray band. Finally, two zones of emission are included to model narrow

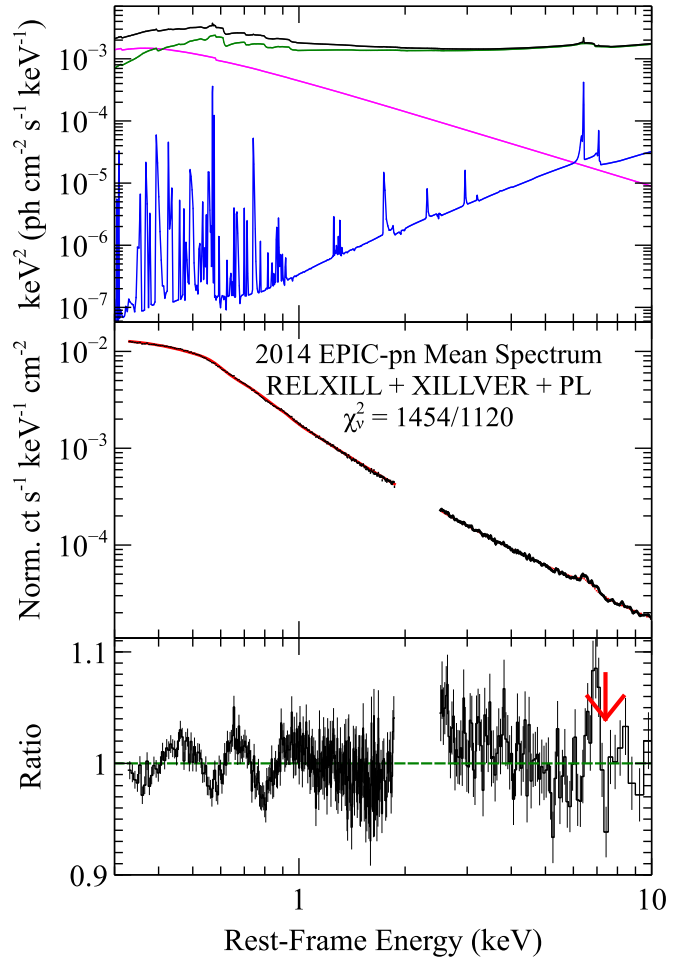


Figure 5. Upper panel: the two-reflector model fitted to the mean EPIC-pn spectrum; the summed contribution is shown in black while the RELXILL, XILLVER and soft power-law components are shown in green, blue and magenta, respectively. Middle panel: the mean EPIC-pn spectrum fitted with the two-reflector model (red). Lower panel: the ratio of the residuals with strong signatures of ionized absorption at ~ 0.5 – 0.9 keV and ~ 7.5 keV (red arrow) and ionized emission at ~ 6.7 – 6.9 keV.

photoionized emission lines, which indicate an average covering factor of $\sim 50\%$.

We now tie both hard- and soft-band models together to generate a single broad-band model which, in XSPEC, takes the form: $\text{TBABS} \times [\text{PL}_{\text{soft}} + (\{\text{PL}_{\text{hard}} + \text{BBODY}\} \times \text{XSTAR}^{\text{abs}}) + \text{XSTAR}^{\text{ems}} + \text{XILLVER}]$. We first focus on the simultaneous rev2670 EPIC-pn + *Nu7* spectrum to be sure that we are free from any complications arising from spectral variability between observations. Due to the more modest spectral resolution <2 keV of the EPIC-pn compared to the RGS, we fix the best-fitting parameters of the ionized absorption/emission grids at the values quoted in Pounds et al. (2016b), just allowing the column densities to vary. Fitting to the 0.3–10 keV EPIC-pn data alone gives a good fit: $\chi^2_{\text{dof}} = 475/471$, with $\Gamma_{\text{hard}} \sim 1.8$ and $\Gamma_{\text{soft}} \sim 3.0$. We then include the simultaneous *NuSTAR* data and extend the fit to 50 keV (although, as mentioned in Section 3.1, the data become background-dominated and noisy >30 keV). Without re-fitting or even re-normalizing, the change in the fit statistic is $\Delta\chi^2 = 583$ for 523 d.o.f. ($\chi^2_{\text{dof}} = 1058/994$), indicating that our fit to the EPIC-pn data predicts the hard X-ray continuum >10 keV well. Allowing the model to re-fit (including a

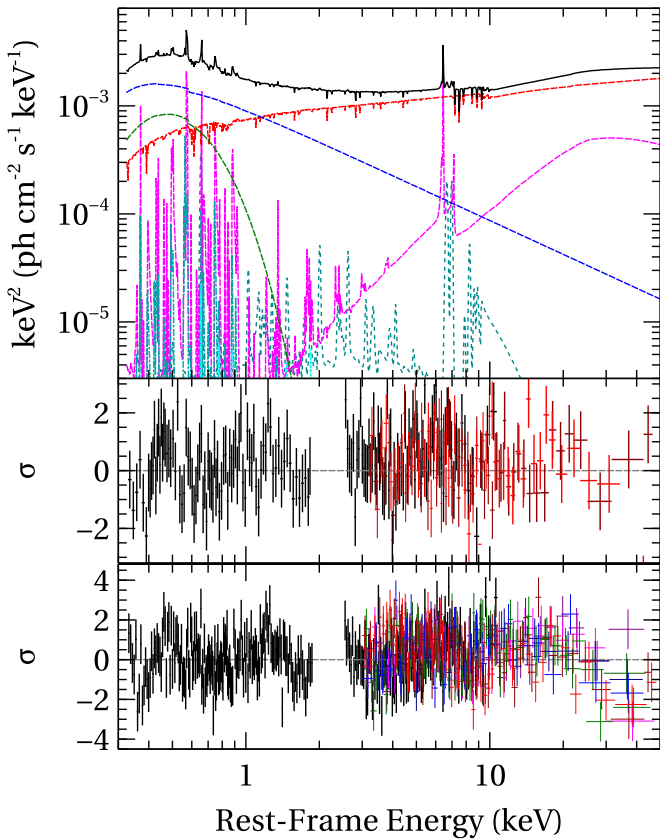


Figure 6. Upper panel: the additive components contributing to the full broad-band model (black): Γ_{hard} (red), Γ_{soft} (blue), blackbody (green), XILLVER (magenta), ionized emission (cyan). Middle panel: $1\text{-}\sigma$ residuals of the rev2670 EPIC-pn (black) + Nu7 (red) 0.3–50 keV spectrum. Lower panel: 1σ residuals of the mean 2014 EPIC-pn (black) + Nu2 (red) + Nu4 (blue) + Nu5 (green) + Nu7 (magenta) spectrum.

floating cross-normalization factor for each *NuSTAR* detector and allowing Γ to vary slightly between the *XMM-Newton* and *NuSTAR* spectra) improves the fit to $\chi^2_{\text{dof}} = 1003/990$. The parameters of the Fe K emission/absorption zones are largely consistent with Pounds et al. (2016a), varying slightly in N_{H} and $\log \xi$, while the reflector (XILLVER) has an emission peak at ~ 6.45 keV ($\log \xi \sim 0.9$; $A_{\text{Fe}} \sim 2.5$). The individual components of the broad-band model are shown in Figure 6 (upper panel) along with the residuals to the best fit (middle panel).

We then fit the model to the high-S/N 2014 mean EPIC-pn + *NuSTAR* spectrum. We include all four *NuSTAR* observations separately with a floating cross-normalization parameter to account for changes in flux over time. Extending the fit to 50 keV results in $\chi^2_{\text{dof}} = 3490/3377$, where we also allow Γ_{hard} to vary between observations (which typically falls within the range $\Gamma_{\text{hard}} = 1.69\text{--}1.94$). Meanwhile, Γ_{soft} remains at a value of ~ 3.1 . We again find that the best-fitting parameters of outflowing ionized absorption components are consistent with those reported in Pounds et al. (2016a, 2016b). The residuals are shown in Figure 6 (lower panel).

Having accounted for the absorption due to both the high-velocity wind apparent in the Fe K band and the lower-velocity/ionization counterparts in the soft X-ray band, we now measure the strength of any relativistic reflection component allowed by the data. We use the model described above but replace the primary power-law component (PL_{hard})

with RELXILL, tying Γ , A_{Fe} , θ and E_{cut} to the corresponding XILLVER values, like in Section 3.2.

In the simultaneous rev2670 + *Nu7* case, this results in a slight improvement to the fit with $\Delta\chi^2 = 25$. The best-fitting reflection fraction is $R \sim 1.1$, while the Fe abundance and photon index remain at values of $A_{\text{Fe}} \sim 3$ and $\Gamma \sim 1.8$, respectively. The RELXILL component is moderately ionized ($\log \xi \sim 1.3$) and predominantly manifests itself by including some degree of broadening on the red side of the Fe K complex. Meanwhile, the XILLVER component models the near-neutral component of Fe K α emission ($\log \xi = 0$).

A very similar result is reached by performing the same test on the 2014 mean EPIC-pn + *NuSTAR* spectrum ($\Delta\chi^2 = 52$), resulting in a modest reflection strength, $R \sim 0.6$, while the photon index and Fe abundance remain unchanged: $\Gamma \sim 1.8$; $A_{\text{Fe}} \sim 3$. The remaining key parameters in the RELXILL model are largely consistent with those reported in Table 2; i.e., $\log \xi \sim 1.2$, $q \sim 3$, $\theta \sim 40$, $r_{\text{in}} < 6$. The black hole spin, a^* , is unconstrained although we find a lower-limit on the high-energy cutoff of $E_{\text{cut}} > 130$ keV.

Finally, we return to check for the presence of highly-ionized absorption in the contemporaneous *NuSTAR* data. In terms of the EPIC-pn analysis, the two absorption grids modeling the highly-ionized two-velocity outflow are highly significant, with a combined contribution to the fit statistic of $\Delta\chi^2 = 42$ (for six additional parameters; meanwhile, the highly-ionized emission and soft-band absorption grids improve the fit by $\Delta\chi^2 = 39$ and $\Delta\chi^2 = 44$, respectively). Zoghbi et al. (2015) detected no significant discrete absorption features in the *NuSTAR* spectrum. We now find, in direct comparison with *XMM-Newton*, including the same two XSTAR absorption zones to the same baseline model fitted to just the contemporaneous *NuSTAR* observations offers a far less significant improvement to the fit statistic, with $\Delta\chi^2 = 9$. As such, even though the highly-ionized outflow is now well established thanks to *XMM-Newton*, we also confirm the main result from Zoghbi et al. (2015) that it was not detectable by *NuSTAR* alone. This demonstrates the importance of long-look observations with *XMM-Newton* in addition to the broad-band coverage of *NuSTAR*.

4. DISCUSSION AND CONCLUSIONS

An extended *XMM-Newton* observation of PG 1211+143 has revealed spectral structure in the Fe K band, unseen in previous (shorter) observations. Utilizing the high throughput of the EPIC-pn, Pounds et al. (2016a) showed that highly-ionized outflow resolved two velocity components ($v_{\text{out}} = 0.129$ and $0.066c$), while an analysis of the high-resolution RGS data in Pounds et al. (2016b) found lower-ionization co-moving counterparts of that dual-velocity flow. Here, we have extended our modeling over a wider energy range, incorporating contemporaneous *NuSTAR* data. The power of this approach—i.e., combining *XMM-Newton* and *NuSTAR* data—has previously been demonstrated in a precise measurement of the higher-energy continuum and thereby helping to disentangle absorption and reflection in a number of AGNs—e.g., NGC 1365 (Risaliti et al. 2013; Walton et al. 2014; Rivers et al. 2015), NGC 5548 (Kaastra et al. 2014; Ursini et al. 2015; Cappi et al. 2016) and PDS 456 (Nardini et al. 2015).

In Section 3.1, we fitted the hard X-ray spectrum with relativistic reflection, following the recent analysis of Zoghbi

et al. (2015). Using the *NuSTAR* data alone, we confirm their solution, finding a steep photon index ($\Gamma \sim 2.4$) and high reflection fraction ($R \sim 2-3$). However, by also including the simultaneous *XMM-Newton* spectrum, just in the 3–10 keV range (which overlaps with the *NuSTAR* bandpass), a harder- Γ /lower- R solution is strongly preferred. Replacing the overlapping *XMM-Newton* data with the high-S/N stacked 2014 EPIC-pn spectrum further tightens the constraints, with $\Gamma = 1.95^{+0.07}_{-0.05}$ and $R = 1.05^{+0.47}_{-0.49}$. Such continuum parameters are now fully consistent with those reported by Pounds et al. (2016a, 2016b), where a detailed analysis of the long-look *XMM-Newton* observation is performed, taking into account the spectral imprints of the outflowing wind.

In Section 3.2, we attempted to fit the broad-band (0.3–50 keV) spectrum with relativistic reflection, finding that, while RELXILL alone cannot simultaneously fit the excess of emission in the soft band and the significant Fe K emission complex, a two-reflector model (comprising a distant reflector and a relativistically blurred reflector) provides a good fit to the simultaneous *rev2670+Nu7* spectrum. However, Figure 5 illustrates the inability of this model to match the spectral features of the stacked 2014 EPIC-pn spectrum. Clearly, a pure reflection model cannot match fine structure in the high-S/N spectrum without significant modification—in particular, strong signatures of ionized absorption at $\sim 0.5-0.9$ keV and ~ 7.5 keV remain in the residuals, along with an excess of ionized emission at $\sim 6.7-6.9$ keV—spectral features resolved by the excellent statistics of the *XMM-Newton* data and identified in Pounds et al. (2016a, 2016b). This emphasizes the value of long-look observations, where the ~ 630 ks stacked EPIC-pn spectrum reveals significant spectral structure, otherwise lost in the statistical noise of shorter observations.

In Section 3.3 we explored an alternative broad-band 0.3–50 keV *XMM-Newton* + *NuSTAR* fit, now including the ionized absorption/emission components required by the *XMM-Newton* spectrum. We find that the model presented in Pounds et al. (2016a, 2016b) extrapolates well to the *NuSTAR* band and, overall, provides an excellent fit to the broad-band X-ray spectrum. Having thus accounted for the various components of the high-velocity outflowing absorber, we note that a contribution of relativistic reflection is allowed by the data, manifesting itself in the form of excess emission just redward of the Fe K complex, although its strength is rather modest ($R \sim 0.6$). Additionally, when fitted to the 0.3–50 keV band, the absorption-dominated model requires a best-fitting photon index of $\Gamma \sim 1.8$, which is significantly different from the value of $\Gamma \sim 2.4$ arrived at by fitting the *NuSTAR* data alone. This conclusion is, of course, supported by our MCMC analysis which shows that a harder- Γ /lower- R solution is preferred when including the simultaneous *XMM-Newton* data, regardless of the assumed continuum model.

Finally, we comment on one of the headline results of the Zoghbi et al. (2015) analysis, namely that the *NuSTAR* spectrum exhibits no evidence of the high-velocity outflow originally reported in Pounds et al. (2003). This claim was based on a line-detection search across the appropriate bandpass with emphasis placed on the ~ 7.1 keV absorption line, first detected in the 2001 observation. The non-detection of that absorption line in the *NuSTAR* spectrum led to the suggestion that the ultra-fast outflow in PG 1211+143 may be transient, or at least highly variable, implying that the

contribution of ultra-fast outflows to feedback could be substantially lower than previously thought.

Pounds et al. (2016a) find that this absorption is indeed variable, depending on both column density and ionization parameter, and had a mean equivalent width around three times smaller during the 2014 *XMM-Newton* observation than it had when first detected in 2001. As such, it is unsurprising that the feature was not significantly detected by a single line search in the *NuSTAR* spectrum. More generally, while a line search has provided a useful method in the past for detecting individual strong resonance lines, a preferred approach is to use self-consistent photoionization models (e.g., with XSTAR), as we do here, which incorporate a physically realistic array of common-velocity lines and absorption edges from various ions (including additional higher-order lines) and imprint appropriate related continuum curvature, for a given N_{H} , ξ and v_{out} . The improvement in the fit statistic is then computed from the summed contributions of all of the absorption features, where several individual weak features may have a significant impact overall (although we do note that even this approach would not have led to a significant detection of the outflow using the contemporaneous *NuSTAR* data alone).

In summary, while Zoghbi et al. (2015) detected no discrete absorption features in the *NuSTAR* spectrum, the extended *XMM-Newton* observations, also in 2014, confirm that not only is the outflow still present, it exhibits more complex spectral structure than previously realized.

In studying the properties of powerful AGN winds, now widely accepted as one of the most important outcomes of the past decade of X-ray observations, we have noted the importance of self-consistent modeling with physically-motivated absorption models which properly account for multiple ions and continuum curvature, and emphasise that (i) finding a common velocity for a line series can provide a highly significant result, and (ii) *XMM-Newton* remains a powerful observatory for detailed, high-resolution spectroscopy, particularly when used in tandem with the broad-band coverage of *NuSTAR*.

This research has made use of the NASA Astronomical Data System (ADS), the NASA Extragalactic Database (NED) and is based on observations obtained with *XMM-Newton*, an ESA science mission with instruments and contributions directly funded by ESA Member States and NASA, and the *NuSTAR* mission, a project led by the California Institute of Technology (Caltech), managed by the Jet Propulsion Laboratory (JPL). APL and SV acknowledge support from STFC consolidated grant ST/K001000/1 and JNR acknowledges financial support via NASA grant NNX15AF12G. We thank an anonymous referee for highly constructive comments which helped improve the clarity of the paper.

Facilities: XMM-Newton (EPIC), NuSTAR.

REFERENCES

- Arnaud, K. A. 1996, in ASP Conf. Ser. 101, *Astronomical Data Analysis Software and Systems V*, ed. G. Jacoby & J. Barnes (San Francisco, CA: ASP), 17
- Blustin, A. J., Page, M. J., Fuerst, S. V., Branduardi-Raymont, G., & Ashton, C. E. 2005, *A&A*, 431, 111
- Cappi, M., De Marco, B., Ponti, G., et al. 2016, *A&A*, 592, 27
- Crenshaw, M. D., Kraemer, S. B., & George, I. M. 2003, *ARA&A*, 41, 117
- Dauser, T., García, J., Walton, D. J., et al. 2016, *A&A*, 590, 76
- Dauser, T., García, J., Wilms, J., et al. 2013, *MNRAS*, 430, 1694

- den Herder, J. W., et al. 2001, *A&A*, 365, 7
- Ferrarese, L., & Merritt, D. 2000, *ApJ*, 539, 9
- García, J., Dauser, T., Lohfink, A., et al. 2014, *ApJ*, 782, 76
- Gebhardt, K. 2000, *ApJ*, 539, 13
- George, I., & Fabian, A. C. 1991, *MNRAS*, 249, 352
- Gofford, J., Reeves, J. N., Tombesi, T., et al. 2013, *MNRAS*, 430, 60
- Grevesse, N., & Sauval, A. J. 1998, *SSRv*, 85, 161
- Haardt, F., & Maraschi, I. 1993, *ApJ*, 413, 507
- Harrison, F. A., Craig, W. W., Christensen, F. E., et al. 2013, *ApJ*, 770, 103
- Jansen, F., et al. 2001, *A&A*, 365, 1
- Kaastra, J. S., Kriss, G. A., Cappi, M., et al. 2014, *Science*, 345, 64
- Kallman, T., Liedahl, D., Osterheld, A., Goldstein, W., & Kahn, S. 1996, *ApJ*, 465, 994
- Kaspi, S., et al. 2002, *ApJ*, 574, 643
- King, A. R. 2003, *ApJL*, 596, L27
- King, A. R. 2010, *MNRAS*, 402, 1516
- Lobban, A. P., Vaughan, S., Pounds, K., & Reeves, J. N. 2016, *MNRAS*, 457, 38
- Madsen, K. K., Harrison, F. A., & Markwardt, C. B. 2015, *ApJS*, 220, 8
- Marziani, P., Sulentic, J. W., Dultzin-Hacyan, D., Calvani, M., & Moles, M. 1996, *ApJS*, 104, 37
- McKernan, B., Yaqoob, T., & Reynolds, C. S. 2007, *MNRAS*, 379, 1359
- Nandra, K., & Pounds, K. A. 1994, *MNRAS*, 268, 405
- Nardini, E., Reeves, J. N., Gofford, J., et al. 2015, *Sci*, 347, 860
- Pounds, K., Lobban, A., Reeves, J., & Vaughan, S. 2016a, *MNRAS*, 457, 2951
- Pounds, K., Lobban, A., Reeves, J., Vaughan, S., & Costa, M. 2016b, *MNRAS*, 459, 4389
- Pounds, K. A. 2014, *MNRAS*, 437, 3221
- Pounds, K. A., & Page, K. L. 2006, *MNRAS*, 372, 1275
- Pounds, K. A., & Reeves, J. N. 2007, *MNRAS*, 374, 823
- Pounds, K. A., & Reeves, J. N. 2009, *MNRAS*, 397, 249
- Pounds, K. A., Reeves, J. N., King, A. R., et al. 2003, *MNRAS*, 345, 705
- Reeves, J. N., O'Brien, P. T., & Ward, M. J. 2003, *ApJ*, 593, 65
- Reynolds, C. S., & Fabian, A. C. 1995, *MNRAS*, 273, 1167
- Risaliti, G., Harrison, F. A., Madsen, K. K., et al. 2013, *Natur*, 494, 449
- Rivers, E., Risaliti, G., Walton, D., et al. 2015, *ApJ*, 804, 107
- Scott, A., Stewart, G., & Mateos, S. 2012, *MNRAS*, 412, 2633
- Shakura, N. I., & Sunyaev, R. A. 1973, *A&A*, 24, 337
- Strüder, L., Briel, U., Dennerl, K., et al. 2001, *A&A*, 365, 18
- Tombesi, F., Cappi, M., Reeves, J. N., et al. 2010, *ApJ*, 742, 44
- Tombesi, F., Cappi, M., Reeves, J. N., et al. 2011, *A&A*, 521, A57
- Ursini, F., Boissay, R., Petrucci, P.-O., et al. 2015, *A&A*, 577, 38
- Verner, D. A., Ferland, G. J., Korista, K. T., & Yakovlev, D. G. 1996, *ApJ*, 465, 487
- Walton, D., Risaliti, G., Harrison, F. A., et al. 2014, *ApJ*, 788, 76
- Willingale, R., Starling, R. L. C., Beardmore, A. P., Tanvir, N. R., & O'Brien, P. T. 2013, *MNRAS*, 431, 394
- Wilms, J., Allen, A., & McCray, R. 2000, *ApJ*, 542, 914
- Zoghbi, A., Miller, J. M., Walton, D. J., et al. 2015, *ApJ*, 799, 24